(Received 7 March 2024, Accepted 18 June 2024, Scheduled 22 June 2024)

# Design of High-Performance Antenna System for High-Speed Railways

Wenrui Zheng[1] and Hui Li[1, 2, *]

[1] School of Information and Communication Engineering, Dalian University of Technology, Dalian 116024, China
[2] Research Institute of Electrical Communication, Tohoku University, 980-8577, Japan

**ABSTRACT:** In this paper, a systematic and efficient method is proposed to collectively synthesize the pattern for multiple antennas on high-speed railways (HSRs) based on pixel structures and $N$-port network, achieving an overall omnidirectional circularly polarized (OCP) pattern over a broad elevation angle. The integration of flush-mounted cavity-backed antennas not only enhances communication quality but also eliminates the undesired aerodynamic drag. Network parameters and radiating features of the $N$-port network based on pixel structures are firstly retained through full-wave simulations. Subsequently, without resorting to extra simulations, the configurations of multiple antennas are precisely synthesized through numerical calculations. The beam direction and beam width of each element can be automatically adjusted, promoting a seamless omnidirectional radiation feature. Following the approach, the proposed antenna thoroughly cover the 5G N41 band (2.515–2.675 GHz), delivering omnidirectional, high-gain, right-hand CP radiation throughout the entire 160 MHz band from $\theta = 50^\circ$ to $100^\circ$. The averaged CP gains and ARs reach 6.09 dBi and 2.36 dB, respectively, within the target region. The antenna system was validated experimentally, with the measured results agreeing well with the simulated ones. Such radiating characteristics perfectly match the established base stations antennas.

## 1. INTRODUCTION

Due to the prevalence of smart terminals in the 5G era, there is an increasing demand for stable connections and low latency on high-speed railways (HSR) communications [1–6]. However, the communication quality between terminal devices in the carriage and external base stations often deteriorates due to the shielding effect of the metallic carriages. Additionally, when the train is running at high speed through various terrains, especially tunnels, viaducts, and cuttings, multipath effects become inevitable [7], and polarization mismatch may occur, which make communication links unstable.

Numerous studies have been reported to enhance HSR's communication performance from the perspective of channel modelling and signal processing [8–13]. In [10], the essential parameters of the propagation channel for train-to-train (T2T) communications in different environments are investigated. In [13], it is suggested that the number of multi-antenna groups should not exceed six. Beyond this limit, adjusting the weights for signal combination becomes significantly more challenging. Besides channel modelling, the characteristics of the relay antennas, particularly their radiation features, play a crucial role in vehicular communications [14–18]. Therefore, deploying high-performance relay antennas on carriages between users and base stations is crucial [19, 20], as indicated in Fig. 1(a).

HSR antennas are expected to provide omnidirectional radiation in the azimuth plane and stably cover a relatively large solid angle in the elevation plane at the same time. In [17], a 3-D antenna system, including a shorted monopole and a drop-shaped monopole, is designed for trains to form omnidirectional radiation in the azimuth plane. In [18], a vertically polarized multi-band antenna mounted on the train's roof is proposed based on modified planar dipole antenna. Although a gain of 4.3–9.8 dBi has been achieved, the beamwidth is too narrow to cover a large area. Additionally, the above-mentioned antennas cannot be fully conformal to the vehicle, resulting in undesired air resistance for the HSR. Furthermore, the use of single linearly polarized antenna raises concerns regarding polarization mismatch and multipath effects. In [21–26], omnidirectional circularly polarized (OCP) antennas have been proposed. Yet they fail to cover a large area in the elevation plane and are not conformal to the train as well.

In order to achieve the desired features, a multi-antenna system is necessary, where each antenna radiates to a specific solid angle with high gain. All antennas collectively cover a wide range of elevation and azimuth angles, which is similar to the sectored base station antennas [27]. Different from base station antennas, HSR antennas cannot physically face different directions due to conformity to the carriage. Therefore, it is challenging to construct a seamless high-gain pattern using the smallest number of antennas with complementary patterns, as indicated in Fig. 1(b). The platform of the vehicle should be considered as well.

One promising approach for antenna pattern synthesis is using pixel antennas [29–41]. By incorporating discrete ports between pixel elements, an impedance matrix describing the characteristics of the antenna can be obtained. Through manipulation of the states between pixels, antenna radiation character-

* Corresponding author: Hui Li (hui.li@dlut.edu.cn).

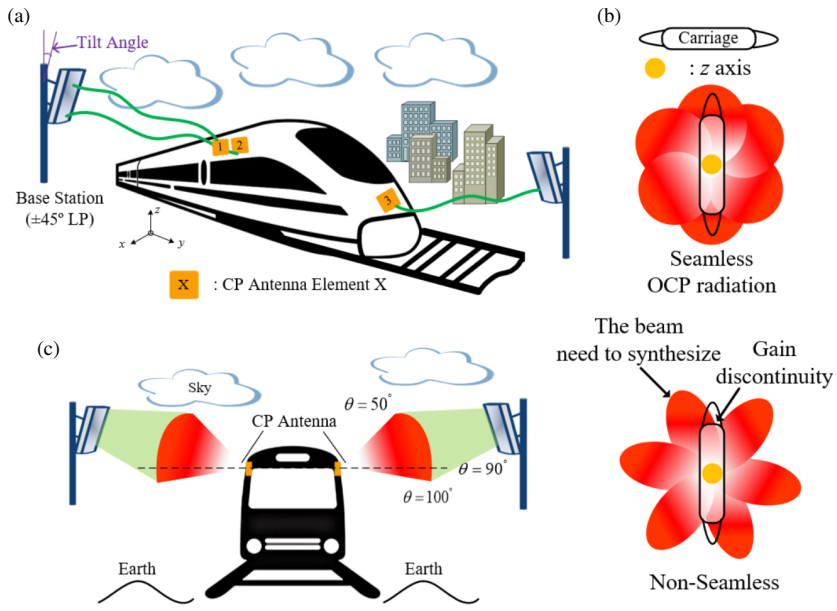


**FIGURE 1**. Sketch of the HSR antenna system. (a) Illustrative sketch; (b) Illustration of seamless and non-seamless radiation patterns' integration; (c) Desired beam width in elevation.

istics can be controlled during optimization, without extensive full-wave simulations. Till now, there are few literatures on joint optimization of multiple antennas utilizing pixels antennas.

In this paper, a systematic scheme to synthesize the overall coverage of multiple antennas is proposed based on pixel antennas. To be flush-mounted with the carriage, dual-layered pixel structures [38] are accommodated in metallic cavities. Full wave simulations are then carried out to provide the impedance matrix and single-port-excited radiation patterns. The pattern synthesis problems are formulated and solved using the multi-objective optimization algorithm NSGA-II [42–44], without trials and errors. Following the approach, besides the omnidirectional pattern in the azimuth plane and large coverage in the elevation plane, circular polarization with averaged CP gain of 6.09 dBi has been achieved as well within the China Mobile N41 band (2.515–2.675 GHz) [45], which can effectively mitigate multipath effects and avoid polarization mismatch.

## 2. DESIGN METHOD

### 2.1. Antenna Configuration

For HSR antennas, to ensure that the antenna structure remains flush with the surface of the carriage, square cavities are excavated from the vehicle, as depicted in Fig. 2(a). Inside the metallic cavity, stepped structures are employed to support the antenna and dielectric radome. A conduit is reserved on the wall of the cavity to accommodate the feeding cable, as indicated by the side view in Fig. 2(b). The dielectric of F4B, with a dielectric constant of 2.2 and a loss tangent of 0.001, is used for the antenna substrate and the radome. The rest of the metallic cavity is filled with air. Since the currents of the proposed cavity-backed antenna are distributed around the cavity itself, a local metallic platform around the antenna's aperture can effectively simulate the antenna's performance on a real carriage, which has been verified in the simulations.

To mimic the real train scenario, the front exterior is inclined by 70° with respect to the horizontal plane. For achieving reliable link with the base station, two antennas (Ant. 1 and Ant. 2) are located at the side of the compartment and one antenna (Ant. 3) is placed at the locomotive, as depicted in Fig. 2(d). Ant. 1 and Ant. 2 are strategically positioned 130 mm apart, facilitating the potential for high isolations. The same set of antenna elements can be applied to the opposite side and the rear of the train to achieve OCP radiation, as illustrated in Fig. 3(a). It's worth noting that the identical antenna element(s) on opposite sides of the carriage don't have mirror-symmetrical radiation features. Instead, the pattern is rotated by 180° in azimuth plane, as depicted in Fig. 3(b). Some key parameters of the structures are provided in the caption of Fig. 2.

Dual-layered pixel structures with high degree of freedoms have been utilized in the cavities. Fig. 2(c) depicts the arrangement of the $4 \times 4$ dual-layered pixel structures. A total of 48 discrete ports are arranged on each antenna element, with the feeding ports designated at the corner for convenient feeding. The connection states between the pixels include shorted and open, as indicated in Fig. 2(c). The number and locations of the shorting strips determine the performance of the HSR antenna system. The port states of the three antennas could be different. By co-optimizing the connection states, a large solid angle in the elevation plane is covered with high gain while maintaining omnidirectional radiation in the azimuth plane. In practical scenarios, power dividers will be utilized to achieve such omnidirectional characteristics.

### 2.2. Antenna Optimization

Once the platform, pixel structures, and $N$-port network are modeled, full-wave simulations can be conducted to obtain

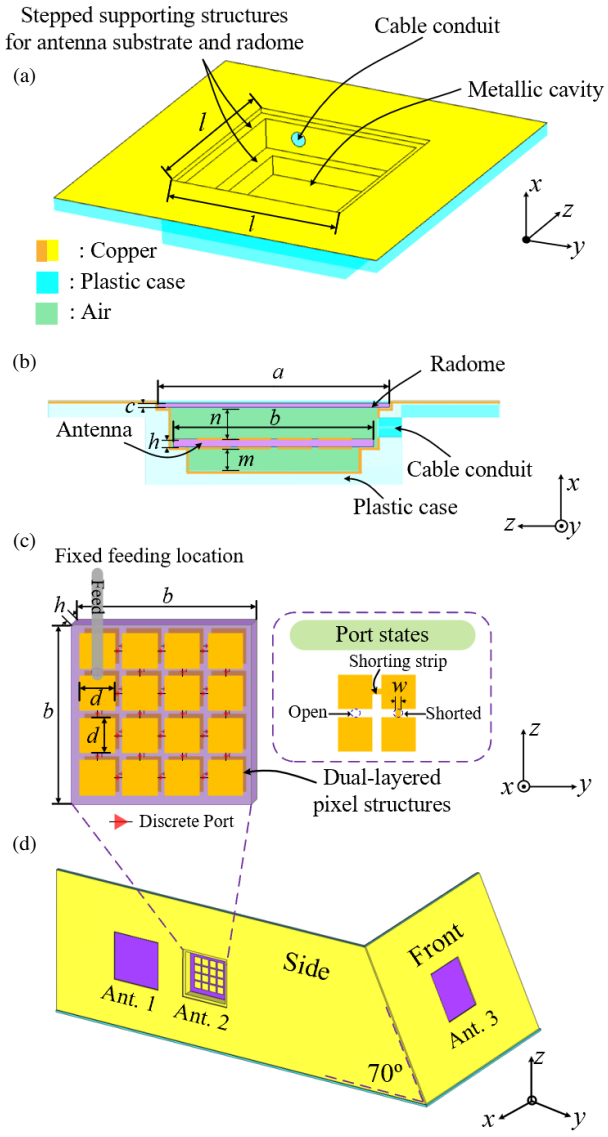


**FIGURE 2**. The configuration of the platform and pixel structures: (a) Perspective view of the metallic cavity; (b) Sectional side view of the cavity; (c) Configuration of the dual-layered pixel structure; (d) Assembled model. (The dimensions are: $l = 84\,\text{mm}$; $a = 82\,\text{mm}$; $b = 71\,\text{mm}$; $c = 1.5\,\text{mm}$; $h = 3\,\text{mm}$; $n = 11.1\,\text{mm}$; $m = 9\,\text{mm}$.)

the impedance matrix and single-port-excited radiation patterns across a specific frequency band in CST Microwave Studio [46]. Since the impacts of radome and supporting structures have been included in the impedance matrix, the antenna performance can be directly optimized using numerical calculation software MATLAB [47], without resorting to additional full-wave simulations. It is for this reason that we are confident in directly housing the pixel structure into the metallic cavity to provide a fully flush appearance. In contrast, adhering to traditional antenna design principles would necessitate a time-consuming process of exhaustive parameter sweeping and investigation.

For an $N$-port network, if the feeding position is determined, the current is determined by the impedance matrix and the voltage vector:

$$[I] = ([Z])^{-1}[V] \tag{1}$$

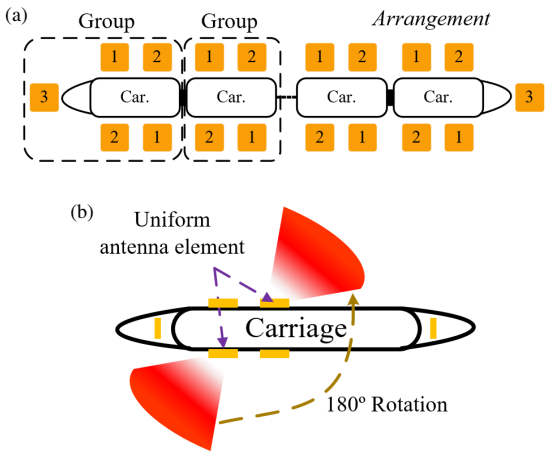


**FIGURE 3**. (a) Antenna element arrangement on a multi-carriage train; (b) Radiation schematic of the same antenna element on different sides.

where $[I]$ and $[Z]$ are the complex current vector and impedance matrix, respectively. $[Z]$ is obtained from full wave simulations. $[V]$ is determined as long as the feeding position in the network is known:

$$[V]_i = \begin{cases} 0, & \text{if } i \neq d, \\ 1 - Z_0[I]_i, & \text{if } i = d. \end{cases} \tag{2}$$

where $Z_0$ represents the characteristic impedance of the coaxial cable. $d$ represents the index of the feeding port in the network. When a port corresponds to a shorted state, the corresponding rows and columns in the initial impedance matrix are retained. In contrast, if a port corresponds to an open state, the corresponding rows and columns are removed from the initial impedance matrix. Hence, the location and number of the shorted ports lead to different impedance matrices, which consequently determine the complex current at each port.

After acquiring the complex port currents, the reflection coefficients can be evaluated by the current at each feeding port:

$$|S_{ii}| = \left|\frac{Z_{\text{in},i} - Z_0}{Z_{\text{in},i} + Z_0}\right| = \left|\frac{\dfrac{1 - Z_0[I]_{ii}}{[I]_{ii}} - Z_0}{\dfrac{1 - Z_0[I]_{ii}}{[I]_{ii}} + Z_0}\right| = |1 - 2Z_0[I]_{ii}| \tag{3}$$

In (4), $[I]_{ii}$ represents the current at port $i$ when port $i$ is excited. When calculating the current at the feeding port, other feeding ports should be terminated with an impedance of $Z_0$. Similarly, transmission coefficients can also be evaluated based on the mutual impedance of the network:

$$|S_{ij}| = \left|\frac{2/Z_0[J]_{ij}}{1 + Z_{ii}/Z_0 + Z_{jj}/Z_0 + \det\begin{vmatrix} Z_{ii}/Z_0 & 1/Z_0[J]_{ij} \\ 1/Z_0[J]_{ij} & Z_{jj}/Z_0 \end{vmatrix}}\right| \tag{4}$$

where $[I]_{ij}$ represents the current at port $j$ when port $i$ is excited. The total electric-field radiation pattern can be computed using linear superposition of single-port-excited patterns as well:

$$\mathbf{E} = \sum_n \frac{[I]_n}{I_0} \mathbf{E}_{0n} \tag{5}$$

where $\mathbf{E}_{0n}$ represents the electric-field pattern when port $n$ is stimulated by a unit current source. $[I_n]$ and $I_0$ are the actual current and the unit current at port $n$, respectively.

In this study, the antennas aim at achieving right-hand circular polarization (RHCP). The RHCP component of the electric-field pattern can be calculated as follows:

$$\mathbf{E}_{\text{right}} = \frac{1}{\sqrt{2}} \left(\mathbf{E}_h + \mathrm{j}\mathbf{E}_v\right) \tag{6}$$

where $\mathbf{E}_h$ and $\mathbf{E}_v$ are the horizontal and vertical components of the electric-field pattern, respectively. Subsequently, the RHCP gain pattern, $\mathbf{G}_{\text{right}}$, can be derived from $\mathbf{E}_{\text{right}}$. With $\mathbf{E}_h$ and $\mathbf{E}_v$, axial-ratio (AR) pattern can be evaluated as well:

$$\mathbf{AR} = \sqrt{\frac{|\mathbf{E}_h|^2 + |\mathbf{E}_v|^2 + |\mathbf{E}_h + \mathbf{E}_v|}{|\mathbf{E}_h|^2 + |\mathbf{E}_v|^2 - |\mathbf{E}_h + \mathbf{E}_v|}} \tag{7}$$

Thus far, all the required performance metrics to describe the HSR antenna system can be evaluated in MATLAB across the band of interest. Therefore, a multi-objective function optimization is formulated:

$$\begin{aligned}
\min_{\mathbf{x}} F_1 =& \frac{1}{P \times D} \sum_{p=1}^{P} \sum_{i=1}^{D} |S_{ii}| \left(f_p, \mathbf{x}\right) \\
&+ w \sum_{p=1}^{P} \sum_{\substack{j=1 \\ j \neq i}}^{D} \sum_{i=1}^{D} \left[|S_{ij}| \left(f_p, \mathbf{x}\right) - T_s\right]^+ \\
F_2 =& \frac{1}{K \times M} \sum_{r=1}^{K} \sum_{p=1}^{M} \left[\max\left(\mathbf{G}^i_{\text{right},p}(f_p, \mathbf{x})\right) - T_c\right]^- \\
&\forall i = 1, 2, 3, \ldots, 2D, \\
&r \in \mathbf{R} \\
F_3 =& \frac{1}{K \times M} \sum_{r=1}^{K} \sum_{p=1}^{M} \min\left(\mathbf{AR}^i_p(f_p, \mathbf{x})\right) \\
&\forall i = 1, 2, 3, \ldots, 2D, \\
&r \in \mathbf{R}
\end{aligned} \tag{8}$$

In (8), $\mathbf{x}$ is the decision variables standing for the port states, with 0 representing an open state and 1 indicating a shorted state. $f_p$ represents the frequency sampling points. $P$ and $D$ stand for the number of frequency samples and external feeding ports, respectively. In $F_1$, the first term optimizes the resonances of all antennas, whereas the second term guarantees the high isolations between these antennas. The operator $[\cdot]^+$ denotes summing up the values above the threshold $T_s$ at each frequency sample. $w$ is a penalty term, which is usually a relatively large value, to prioritize the isolation requirements of the antenna system.

$F_2$ incorporates the RHCP gain of the antenna system for each solid angle within the target region $\mathbf{R}$. $\mathbf{R}$ covers $\theta \in [50°, 100°]$ and $\varphi \in [0°, 360°]$ so that omnidirectional radiation is covered by the whole antenna system. The range of the elevation angles aligns with the beam range of the base station antenna, with the radiation towards the ground and the sky minimized, as illustrated in Fig. 1(c). $K$ represents the number of sampled points within $\mathbf{R}$. Unlike $P$, $M$ signifies the number of frequency points examined during the evaluation of far-field characteristics. Since the computational resources required to evaluate radiation characteristics significantly outweigh those needed to assess $S$-parameters, $M$ is typically less than $P$. The operator $[\cdot]^-$ denotes summing up the values below the threshold $T_c$ at each frequency sample, where $T_c$ serves as a threshold to prevent excessive gain optimization at specific solid angles. The superscript $i$ on $\mathbf{G}$ indicates the index of the feeding port. Through the minimization of $F_2$, OCP radiation within a large elevation angle can be effectively realized. Similarly, $F_3$ minimizes the averaged $\mathbf{AR}$ within the target region.

## 3. DESIGN PROCESS AND SIMULATION RESULTS

### 3.1. Design Process

Since three antennas are collectively optimized, there are 144 discrete ports in total. By conducting full-wave simulations on the 144-port network, the impedance matrix with the dimension of $144 \times 144$ and 144 single-port-excited radiation patterns can be obtained across the band of interest. With these two critical data sets, optimization can be carried out in MATLAB using the multi-objective function in (8).

During the optimization, $D$ is set to 3 for three independent antenna elements. During the calculation of network parameters, the frequency range $f_p$ is set from 2.5 GHz to 2.7 GHz with a step size of 5 MHz, leading to a total sampling points of $P = 41$. To evaluate the far-field patterns, we select three sampling points ($M = 3$) at 2.515 GHz, 2.595 GHz, and 2.675 GHz. The far-field angle step is set to 10°, resulting in a total of 216 samples for one pattern ($K = 216$). Threshold $T_s$ and penalty term $w$ are set to 0.031 (around $-30$ dB) and 1000, respectively, to ensure high isolations. $T_c$ is chosen to be 6 dBi to achieve high RHCP gain.

The number of decision variables in NSGA-II is 141, representing the port states excluding the three predefined feeding ports. The population size is selected to be 300, with crossover and mutation probabilities being 1 and 0.01, respectively. The optimization converges in approximately 40 minutes on a desktop computer equipped with an i9-12900K CPU. As a result, a Pareto front is obtained, illustrating the "trade-off" among impedance bandwidth, gain, and axial ratio, as shown in Fig. 4.

By examining the objective functions in (8) quantitatively, it reveals that $F_1$ values below 0.3 (around $-10$ dB) indicate good impedance bandwidth and high isolation levels. $F_2$ values be-

low 0.5 imply that the RHCP gains are above 6 dBi for most solid angles within the target area. $F_3$ values below 3 suggest that the AR within the target range largely fulfill the criteria for circular polarization. Based on these criteria, a balanced point is selected with its coordinates at [0.16, 0.36, 2.26], as marked by the red pentagram in Fig. 4. The configurations of the corresponding three antennas are depicted in Fig. 5. The positions of the feeding cables are marked to ascertain the orientation of the substrate. Ant. 1, Ant. 2, and Ant. 3 utilize 24, 20, and 14 shorting strips, respectively.

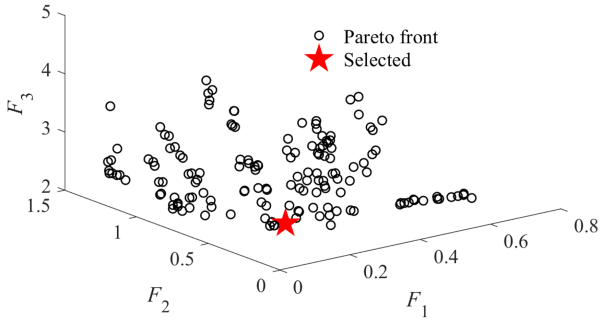


**FIGURE 4**. 3-D Pareto front with the selected balanced result for the HSR antenna system considering the "trade-offs" between the $S$-parameters ($F_1$), the RHCP gain ($F_2$) and the axial ratio ($F_3$).

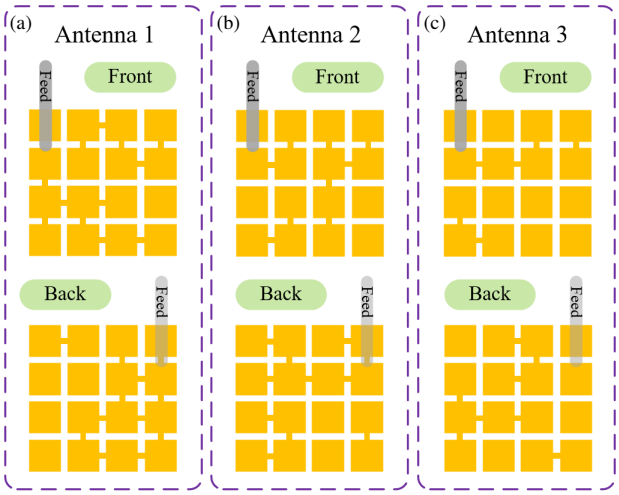


**FIGURE 5**. Front and back view of the optimized antennas.

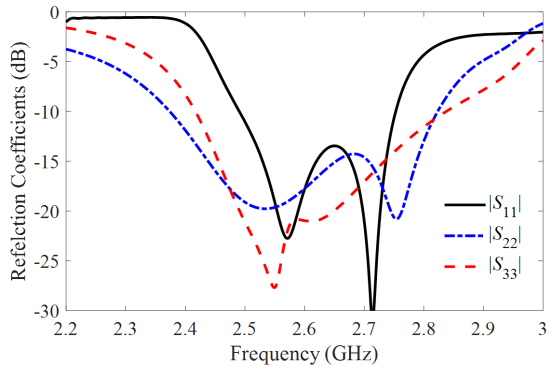


**FIGURE 6**. Simulated reflection coefficients of the proposed HSR antenna system.

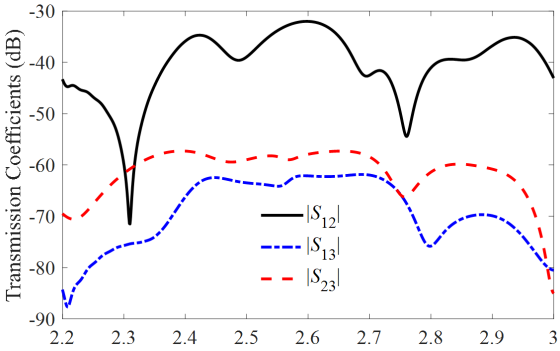


**FIGURE 7**. Simulated transmission coefficients of the proposed HSR antenna system.

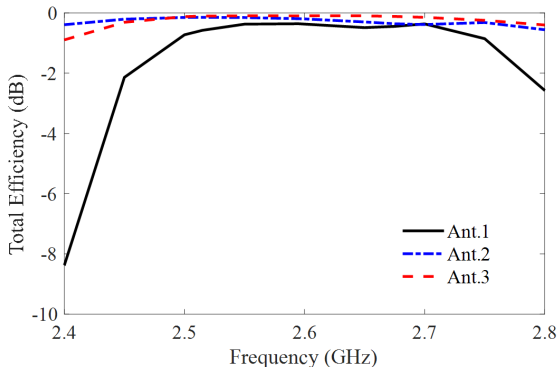


**FIGURE 8**. Simulated total efficiencies of the proposed HSR antenna system.

### 3.2. Simulation Results

Full wave simulations are carried in the transient domain solver of CST to validate the final performance of the proposed HSR antenna system. Fig. 6 depicts the reflection coefficients of the three antennas, all covering the target frequency band from 2.515 GHz to 2.675 GHz. The specific $-10$ dB bandwidths for Ant. 1, Ant. 2, and Ant. 3 are 260 MHz (2.49–2.75 GHz), 410 MHz (2.41–2.82 GHz), and 470 MHz (2.37–2.84 GHz), respectively. Fig. 7 presents the isolations among the three antennas, which are all above 30 dB, indicating little mutual interference among the antenna elements. The total efficiencies of the antennas are provided in Fig. 8. The averaged efficiencies of Ant. 1, Ant. 2, and Ant. 3 within the target band are $-0.43$ dB, $-0.22$ dB, and $-0.10$ dB, respectively.

To illustrate the individual contribution of each antenna to the total coverage, Fig. 9 shows the RHCP gain patterns of the three different antenna elements. To illustrate the omnidirectional coverage, each display includes the antenna pattern in its original positions, as well as the pattern in its corresponding rotated position on the opposite side of the vehicle. The radiation patterns are shown at frequencies of 2.515 GHz, 2.595 GHz, and 2.675 GHz. The integrated radiation patterns, which combine the patterns of six antenna elements, are also calculated and revealed. High gain has been achieved with OCP radia-

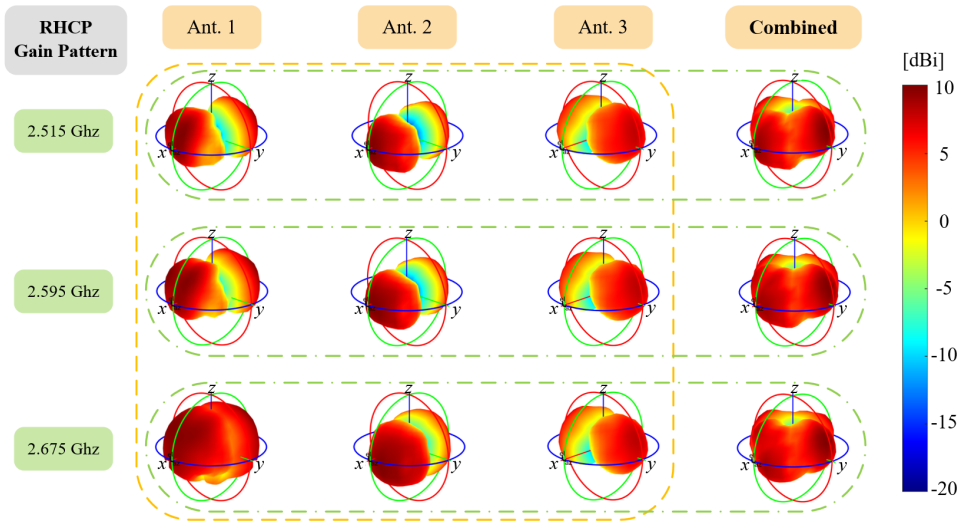


**FIGURE 9**. RHCP gain patterns of the three antenna elements and the combined one.

tions in wide elevation angles. The maximum gains of 8.06 dBi, 8.18 dBi, and 8.25 dBi are obtained for Ant. 1, Ant. 2, and Ant. 3, respectively.

The current distributions on the front and back pixels of the three antennas are presented in Fig. 10. It is evident that each antenna element exhibits unique current distributions, with all the pixel units fully utilized, resulting in varying beam directions and bandwidths. The radiation of the antenna unit is mainly determined by the current distributions on the pixels at both sides. The currents on the metallic cavity contribute slightly to the radiation as well.

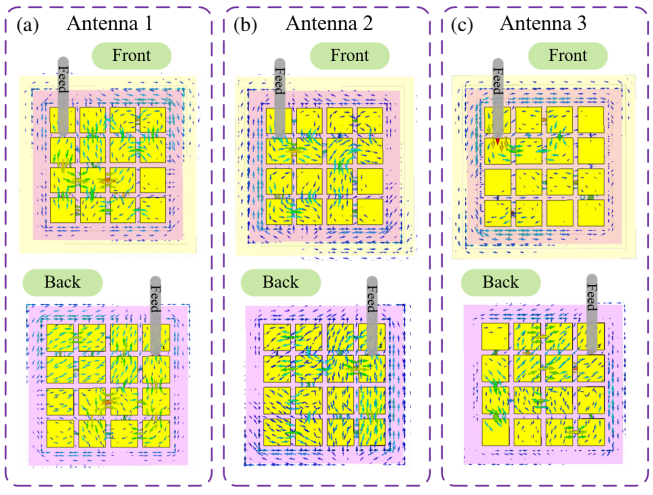


**FIGURE 10**. Current distributions of the optimized antennas.

To provide a more quantitative view of the patterns, the combined 2-D radiation patterns on the horizontal planes at various elevation angles within the target region are displayed in Figs. 11(a)–(c). As can be observed, the radiation characteristics are relatively stable across the entire target band, with the RHCP gain maintaining above 3 dBi. The averaged CP gains within the target region reach 5.96 dBi, 6.20 dBi, and 6.11 dBi, respectively, at 2.515 GHz, 2.595 GHz, and 2.675 GHz, indicating stable link with the base stations. Fig. 12 illustrates the axial ratio of the proposed antenna system in a similar manner. The averaged ARs within the target area reach 2.41 dB, 2.08 dB, and 2.59 dB at 2.515 GHz, 2.595 GHz, and 2.675 GHz, respectively, effectively mitigating multipath effects and avoiding polarization mismatch.

It should be noted that Ant. 1 and Ant. 2, located on the same plane, have been collectively optimized with different main lobe directions, as shown in Fig. 9. Despite some inevitable overlap of radiation patterns along the $x$-axis, their different main lobe directions are beneficial for seamless CP radiation together with Ant. 3. To highlight the necessity of 6-beam synthesis, Figs. 11(d)–(e) present the combined results at 2.595 GHz without Ant. 2 or Ant. 1 respectively for reference. It can be observed that the variations of the RHCP gain significantly increase. Consequently, the axial ratio will also exhibit spatial discontinuities, deviating from the initial requirements for OCP radiation.

## 4. EXPERIMENTS AND DISCUSSIONS

To validate the performance of the proposed high-gain HSR antenna system with OCP radiation within a large elevation angle, a prototype was fabricated, as shown in Fig. 13. The antenna platform, featuring three cavities, was built using 3D printing technology, ensuring consistency with structures in the simulation. To construct a metallic platform, the surface of the 3D-printed structure was covered by copper foil, which mimics a realistic train platform. Three hand-made $\lambda/4$ baluns, as given in Fig. 13(a), were employed to ensure balanced feeding for each antenna element, reducing the radiation due to the outer conductor of the coaxial cable.

$S$-parameters of the antennas mounted on the HSR were measured using Ceyear 3672C vector network analyzer, as depicted in Fig. 13(c). The measured $S$-parameters are given in

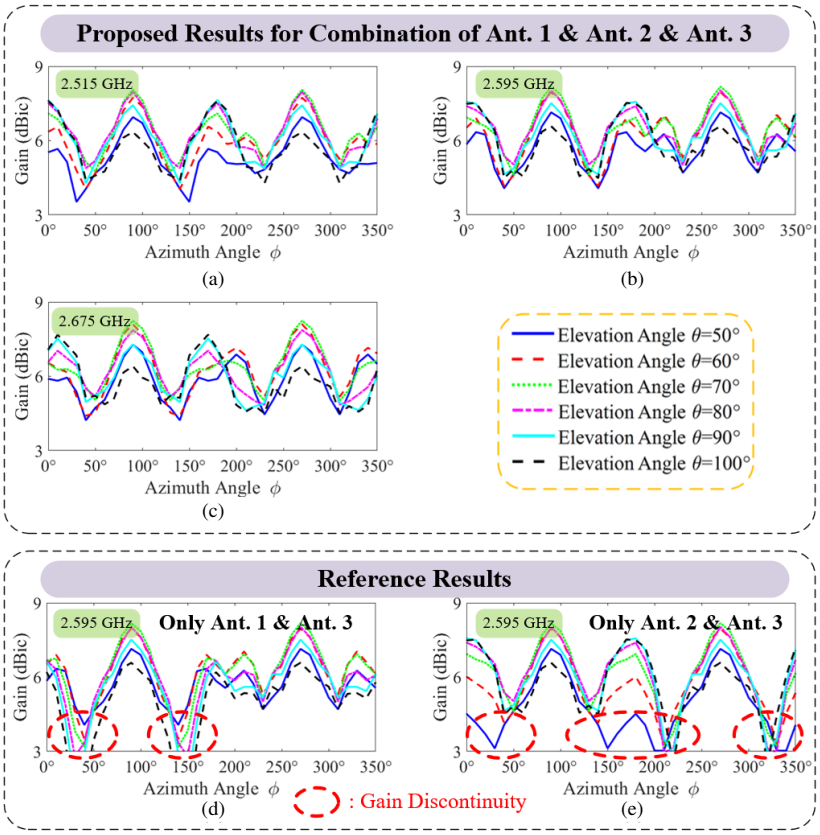


**FIGURE 11**. Simulated two-dimensional depiction of horizontal planes' RHCP gains at various elevation angles within the target omnidirectional region for the combined pattern: (a)–(c) Proposed results; (d)–(e) Reference results.

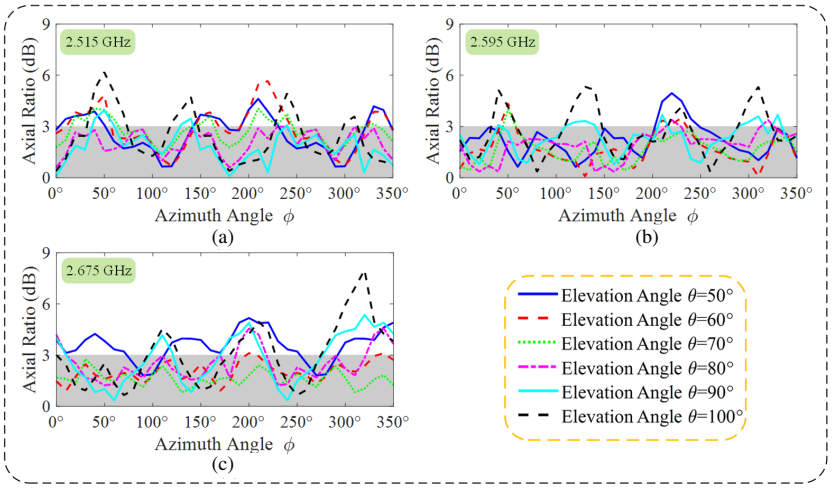


**FIGURE 12**. Simulated two-dimensional depiction of horizontal planes' axial ratios at various elevation angles within the target omnidirectional region for the combined pattern.

Fig. 14. All the three antennas resonated well at the target band, providing the −10 dB bandwidths of 280 MHz (2.48–2.76 GHz), 570 MHz (2.28–2.85 GHz), and 350 MHz (2.46–2.81 GHz), respectively, for Ant. 1, Ant. 2, and Ant. 3. Compared with the simulated results, the bandwidth of Ant. 2 was expanded, while Ant. 3 shifted slightly to the higher band. The discrepancy might be due to the assembly tolerance and the influence of the cables. The measured transmission coefficients were all above 35 dB over the target band.

The radiation pattern test of the antenna was conducted using a local metallic plate serving as a substitute for a real carriage in an anechoic chamber, since the currents were only distributed around the cavity itself. Due to the constraints of the testing site, the entire casing was divided into two sections for the con-

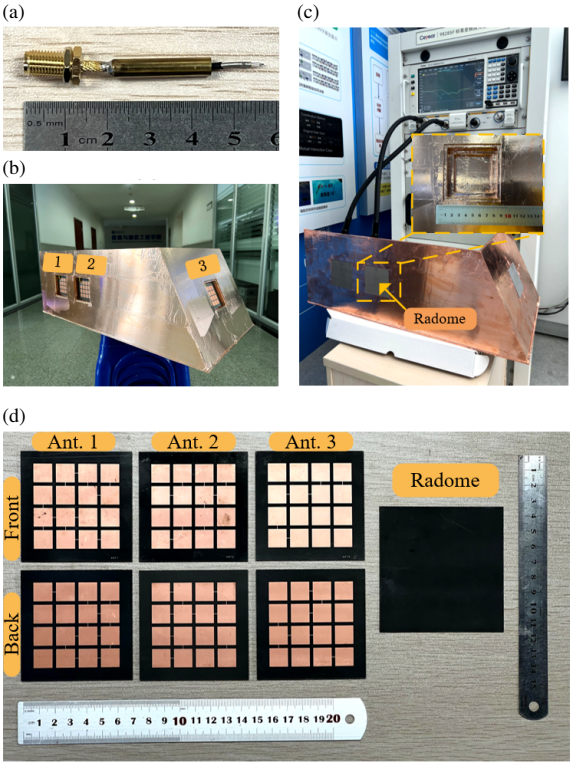


**FIGURE 13**. Prototype of the proposed HSR antenna system. (a) Handmade $\lambda/4$ balun; (b) The casing without radomes; (c) The casing with radomes and the measurement setup for $S$-parameters; (d) Prototype of the three antenna elements and the radome.

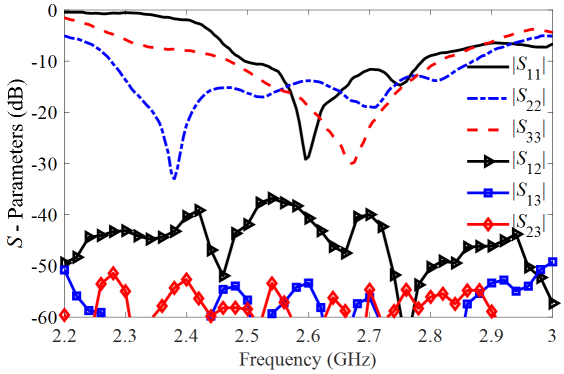


**FIGURE 14**. Measured $S$-parameters of the proposed HSR antenna system.

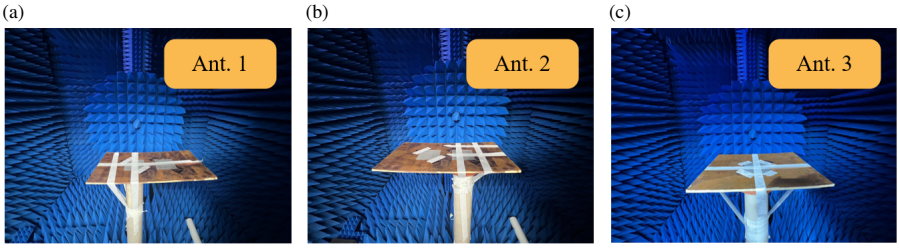


**FIGURE 15**. Measurement setups in the anechoic chamber for the three antennas.

venience of the measurement. One section included both Ant. 1 and Ant. 2, while the other consisted solely of Ant. 3. The measurement setups for those three antennas were shown in Fig. 15. Given the high isolation between the Ant. 1, 2 and the Ant. 3, the separate measurement would not affect the accuracy of the results.

The measured RHCP gain patterns of the three antennas were processed through coordinate rotation and then combined so that they can be compared with those in the simulations, as depicted in Fig. 16. It was observed that the measured averaged CP gains within the target region were 5.46 dBi, 6.31 dBi, and 5.75 dBi at 2.515 GHz, 2.595 GHz, and 2.675 GHz, respectively, which generally agreed well with the simulated values. The slightly lower averaged gain could be attributed to the variations in measured beam directions and beam width, which result in lower gains at certain angles. However, the maximum gains were similar for the simulated and measured results.

The measured AR patterns were depicted in Fig. 17, with the averaged ARs within the target area being 2.42 dB, 2.29 dB, and 2.80 dB at 2.515 GHz, 2.595 GHz, and 2.675 GHz, respectively, showing good agreement with the simulation results as well. The measured total efficiencies are presented in Fig. 18. The average in-band efficiency reached around $-0.3$ dB for each antenna element, which was slightly lower than the simulated ones attributed to the cable loss.

In general, this work aims at providing a systematic design method rather than a fixed design. In real-world engineering applications, it is necessary to consider factors such as the streamlined outer surface of a train and various electrical devices. In such complex environment, the proposed method can

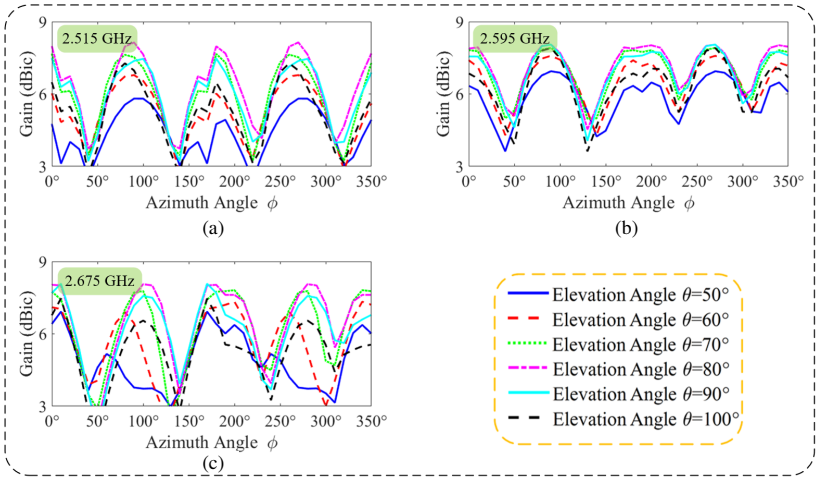


**FIGURE 16**. Measured two-dimensional depiction of horizontal planes' RHCP gains at various elevation angles within the target omnidirectional region for the combined pattern.

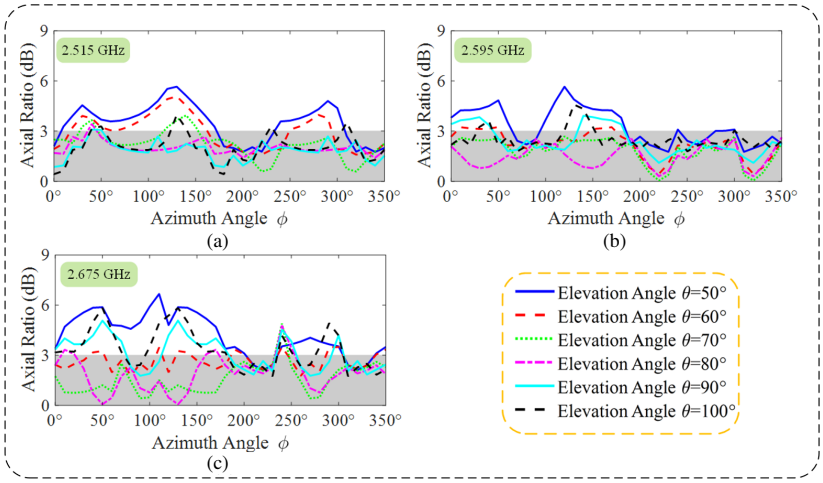


**FIGURE 17**. Measured two-dimensional depiction of horizontal planes' axial ratios at various elevation angles within the target omnidirectional region for the combined pattern.

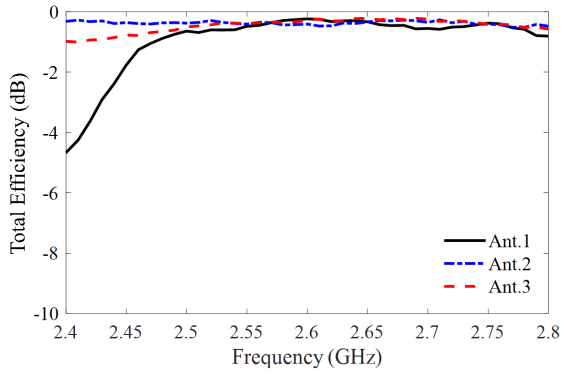


**FIGURE 18**. Measured total efficiency of the proposed HSR antenna system.

still effectively guide antenna design by incorporating all these factors into the initial multi-port full-wave simulation, allowing the optimizer to automatically generate the most suitable antenna geometry for certain environment. This is exactly the advantage of the proposed method.

## 5. CONCLUSION

In this paper, a systematic and efficient method has been proposed to collectively synthesize the pattern for multiple antennas. Following the method, three different cavity-backed antenna elements have been successfully synthesized for HSR applications, without any trial-and-error process. By providing complementary patterns, a high gain antenna system with an overall OCP pattern within a large elevation angle has been obtained. The antenna system can be flush-mounted on the carriage platform, providing stable communication links for vehicles at high speeds. The method can be potentially applied to various platforms for achieving desired complementary patterns.

## ACKNOWLEDGEMENT

This work at Dalian University of Technology was sponsored by the National Natural Science Foundation of China (NSFC) under Grant No. 62371089.

## REFERENCES

[1] Noh, G., B. Hui, and I. Kim, "High speed train communications in 5G: Design elements to mitigate the impact of very high mobility," *IEEE Wireless Communications*, Vol. 27, No. 6, 98–106, Dec. 2020.

[2] Zhang, X., Y. Niu, S. Mao, Y. Cai, R. He, B. Ai, Z. Zhong, and Y. Liu, "Resource allocation for millimeter-wave train-ground communications in high-speed railway scenarios," *IEEE Transactions on Vehicular Technology*, Vol. 70, No. 5, 4823–4838, May 2021.

[3] Li, P., Y. Niu, H. Wu, Z. Han, B. Ai, N. Wang, and Z. Zhong, "RIS-assisted scheduling for high-speed railway secure communications," *IEEE Transactions on Vehicular Technology*, Vol. 72, No. 3, 3488–3501, Mar. 2023.

[4] Gao, M., B. Ai, Y. Niu, W. Wu, P. Yang, F. Lyu, and X. Shen, "Efficient hybrid beamforming with anti-blockage design for high-speed railway communications," *IEEE Transactions on Vehicular Technology*, Vol. 69, No. 9, 9643–9655, Sep. 2020.

[5] Sindhuja, P., Y. Kuwahara, K. Kumaki, and Y. Hiramatsu, "A design of vehicular GPS and LTE antenna considering the vehicular body effects," *Progress In Electromagnetics Research C*, Vol. 53, 75–87, 2014.

[6] Khan, B., M. Berg, S. Rousu, and A. Pärssinen, "Beam switchable vehicular antenna for increased communication range," *Progress In Electromagnetics Research M*, Vol. 66, 203–213, 2018.

[7] Paulraj, A. J. and C. B. Papadias, "Space-time processing for wireless communications," *IEEE Signal Processing Magazine*, Vol. 14, No. 6, 49–83, Nov. 1997.

[8] Ai, B., X. Cheng, T. Kürner, Z.-D. Zhong, K. Guan, R.-S. He, L. Xiong, D. W. Matolak, D. G. Michelson, and C. Briso-Rodriguez, "Challenges toward wireless communications for high-speed railway," *IEEE Transactions on Intelligent Transportation Systems*, Vol. 15, No. 5, 2143–2158, Oct. 2014.

[9] He, R., Z. Zhong, B. Ai, and J. Ding, "An empirical path loss model and fading analysis for high-speed railway viaduct scenarios," *IEEE Antennas and Wireless Propagation Letters*, Vol. 10, 808–812, 2011.

[10] Unterhuber, P., M. Walter, U.-C. Fiebig, and T. Kürner, "Stochastic channel parameters for train-to-train communications," *IEEE Open Journal of Antennas and Propagation*, Vol. 2, 778–792, 2021.

[11] Ling, J., X. Hou, X. Zhao, J. Li, D. Wang, and X. You, "On the performance of a double-sided massive D-MIMO system for high-speed trains communications," *IEEE Transactions on Vehicular Technology*, Vol. 72, No. 10, 13 298–13 313, Oct. 2023.

[12] Zhou, T., Y. Qiao, S. Salous, L. Liu, and C. Tao, "Machine learning-based multipath components clustering and cluster characteristics analysis in high-speed railway scenarios," *IEEE Transactions on Antennas and Propagation*, Vol. 70, No. 6, 4027–4039, Jun. 2022.

[13] Luo, W., X. Fang, M. Cheng, and Y. Zhao, "Efficient multiple-group multiple-antenna (MGMA) scheme for high-speed railway viaducts," *IEEE Transactions on Vehicular Technology*, Vol. 62, No. 6, 2558–2569, Jul. 2013.

[14] Arya, A. K., S. Han, and S. Kim, "Review of antennas for railway communications," *Journal of Electromagnetic Engineering and Science*, Vol. 23, No. 2, 90–100, 2023.

[15] Zou, L., Z. Li, L. Liu, and J. Wang, "A design method for a leaky-wave system with uniform field coverage and broadside radiation for a vacuum-tube ultra-high-speed train," *IEEE Transactions on Antennas and Propagation*, Vol. 70, No. 10, 9936–9941, Oct. 2022.

[16] Kwon, O.-Y., R. Song, and B.-S. Kim, "A fully integrated shark-fin antenna for MIMO-LTE, GPS, WLAN, and WAVE applications," *IEEE Antennas and Wireless Propagation Letters*, Vol. 17, No. 4, 600–603, Apr. 2018.

[17] Navarro-Méndez, D. V., L. F. Carrera-Suárez, D. Sánchez-Escuderos, M. Cabedo-Fabrés, M. Baquero-Escudero, M. Gallo, and D. Zamberlan, "Wideband double monopole for mobile, WLAN, and C2C services in vehicular applications," *IEEE Antennas and Wireless Propagation Letters*, Vol. 16, 16–19, 2017.

[18] Cui, J., A. Zhang, and X. Chen, "An omnidirectional multiband antenna for railway application," *IEEE Antennas and Wireless Propagation Letters*, Vol. 19, No. 1, 54–58, Jan. 2020.

[19] Addali, K. M., A. Benmimoune, F. A. Khasawneh, A. M. Saied, and M. Kadoch, "Dual-backhaul links in LTE-A mobile relay system for high-speed railways," in *2016 IEEE 4th International Conference on Future Internet of Things and Cloud Workshops (FiCloudW)*, 98–102, Vienna, Austria, 2016.

[20] Lin, S.-H., Y. Xu, L. Wang, and J.-Y. Wang, "Coverage analysis and chance-constrained optimization for HSR communications with carrier aggregation," *IEEE Transactions on Intelligent Transportation Systems*, Vol. 23, No. 9, 15 107–15 120, Sep. 2022.

[21] Gao, S. S., Q. Luo, and F. Zhu, *Circularly Polarized Antennas*, Wiley, Hoboken, NJ, USA, 2014.

[22] Sakaguchi, K. and N. Hasebe, "A circularly polarized omnidirectional small helical antenna," in *1995 Ninth International Conference on Antennas and Propagation, ICAP'95 (Conf. Publ. No. 407)*, Vol. 1, 492–495, Apr. 1995.

[23] Li, B., S.-W. Liao, and Q. Xue, "Omnidirectional circularly polarized antenna combining monopole and loop radiators," *IEEE Antennas and Wireless Propagation Letters*, Vol. 12, 607–610, May 2013.

[24] Pan, Y. M., K. W. Leung, and K. Lu, "Omnidirectional linearly and circularly polarized rectangular dielectric resonator antennas," *IEEE Transactions on Antennas and Propagation*, Vol. 60, No. 2, 751–759, Feb. 2012.

[25] Shi, J., X. Wu, X. Qing, and Z. N. Chen, "An omnidirectional circularly polarized antenna array," *IEEE Transactions on Antennas and Propagation*, Vol. 64, No. 2, 574–581, Feb. 2016.

[26] Wu, D., X. Chen, L. Yang, G. Fu, and X. Shi, "Compact and low-profile omnidirectional circularly polarized antenna with four coupling arcs for UAV applications," *IEEE Antennas and Wireless Propagation Letters*, Vol. 16, 2919–2922, 2017.

[27] "Cellular network," https://en.wikipedia.org/wiki/Cellular_network.

[28] Sugimura, D., M. Arai, K. Sakaguchi, K. Araki, and T. Sotoyama, "A study on beam tilt angle of base station antennas for base station cooperation systems," in *2011 IEEE 22nd International Symposium on Personal, Indoor and Mobile Radio Communications*, 2374–2378, Toronto, ON, Canada, Sep. 2011.

[29] Pringle, L. N., P. H. Harms, S. P. Blalock, G. N. Kiesel, E. J. Kuster, P. G. Friederich, R. J. Prado, J. M. Morris, and G. S. Smith, "A reconfigurable aperture antenna based on switched links between electrically small metallic patches," *IEEE Transactions on Antennas and Propagation*, Vol. 52, No. 6, 1434–

1445, Jun. 2004.

[30] Rodrigo, D., B. A. Cetiner, and L. Jofre, "Frequency, radiation pattern and polarization reconfigurable antenna using a parasitic pixel layer," *IEEE Transactions on Antennas and Propagation*, Vol. 62, No. 6, 3422–3427, Jun. 2014.

[31] Besoli, A. G. and F. D. Flaviis, "A multifunctional reconfigurable pixeled antenna using MEMS technology on printed circuit board," *IEEE Transactions on Antennas and Propagation*, Vol. 59, No. 12, 4413–4424, Dec. 2011.

[32] Yuan, X., Z. Li, D. Rodrigo, H. S. Mopidevi, O. Kaynar, L. Jofre, and B. A. Cetiner, "A parasitic layer-based reconfigurable antenna design by multi-objective optimization," *IEEE Transactions on Antennas and Propagation*, Vol. 60, No. 6, 2690–2701, Jun. 2012.

[33] Li, Z., D. Rodrigo, L. Jofre, and B. A. Cetiner, "A new class of antenna array with a reconfigurable element factor," *IEEE Transactions on Antennas and Propagation*, Vol. 61, No. 4, 1947–1955, Apr. 2013.

[34] Lotfi, P., S. Soltani, and R. D. Murch, "Printed endfire beam-steerable pixel antenna," *IEEE Transactions on Antennas and Propagation*, Vol. 65, No. 8, 3913–3923, Aug. 2017.

[35] Jiang, F., S. Shen, C.-Y. Chiu, Z. Zhang, Y. Zhang, Q. S. Cheng, and R. Murch, "Pixel antenna optimization based on perturbation sensitivity analysis," *IEEE Transactions on Antennas and Propagation*, Vol. 70, No. 1, 472–486, Jan. 2022.

[36] Rao, J., Y. Zhang, S. Tang, Z. Li, S. Shen, C.-Y. Chiu, and R. Murch, "A novel reconfigurable intelligent surface for wide-angle passive beamforming," *IEEE Transactions on Microwave Theory and Techniques*, Vol. 70, No. 12, 5427–5439, Dec. 2022.

[37] Zhang, Y., Z. Han, S. Tang, S. Shen, C.-Y. Chiu, and R. Murch, "A highly pattern-reconfigurable planar antenna with 360° single- and multi-beam steering," *IEEE Transactions on Antennas and Propagation*, Vol. 70, No. 8, 6490–6504, Aug. 2022.

[38] Zheng, W. and H. Li, "Designing antennas with quasi-isotropic radiation patterns using pixel structures," *IEEE Transactions on Antennas and Propagation*, Vol. 71, No. 10, 7813–7823, Oct. 2023.

[39] Zheng, W., Y. Pan, and H. Li, "Synthesis of filtering terminal antennas based on N-port networks," *IEEE Transactions on Antennas and Propagation*, Vol. 71, No. 10, 8278–8283, Oct. 2023.

[40] Soltani, S., P. Lotfi, and R. D. Murch, "Design and optimization of multiport pixel antennas," *IEEE Transactions on Antennas and Propagation*, Vol. 66, No. 4, 2049–2054, Apr. 2018.

[41] Jiang, F., Z. Zhang, M. Li, S. Shen, C.-Y. Chiu, Y. Zhang, Q. S. Cheng, and R. Murch, "Multiport pixel antenna optimization using characteristic mode analysis and sequential feeding port search," *IEEE Transactions on Antennas and Propagation*, Vol. 70, No. 10, 9160–9174, Oct. 2022.

[42] Deb, K., A. Pratap, S. Agarwal, and T. Meyarivan, "A fast and elitist multiobjective genetic algorithm: NSGA-II," *IEEE Transactions on Evolutionary Computation*, Vol. 6, No. 2, 182–197, Apr. 2002.

[43] Yang, J. O., Q. R. Yuan, F. Yang, H. J. Zhou, Z. P. Nie, and Z. Q. Zhao, "Synthesis of conformal phased array with improved NSGA-II algorithm," *IEEE Transactions on Antennas and Propagation*, Vol. 57, No. 12, 4006–4009, Dec. 2009.

[44] Jayaprakasam, S., S. K. A. Rahim, C. Y. Leow, T. O. Ting, and A. A. Eteng, "Multiobjective beampattern optimization in collaborative beamforming via NSGA-II with selective distance," *IEEE Transactions on Antennas and Propagation*, Vol. 65, No. 5, 2348–2357, May 2017.

[45] everythingRF, "5G frequency spectrum in China," Available: hhttps://www.everythingrf.com/community/5g-frequency-spectrum-in-china.

[46] CST Studio Suite, CST Microwave Studio, Dearborn, MI, USA, 2021.

[47] Makarov, S. N., *Antenna and EM Modeling with MATLAB*, Wiley, New York, NY, USA, 2002.